ENGINEERING

Ultrathin micromolded 3D scaffolds for high-density photoreceptor layer reconstruction

In-Kyu Lee[1,2†], Allison L. Ludwig[3,4,5†], M. Joseph Phillips[4,5†], Juhwan Lee[1,2†], Ruosen Xie[2,6], Benjamin S. Sajdak[5,7], Lindsey D. Jager[4], Shaoqin Gong[2,5,6*], David M. Gamm[3,4,5,8*], Zhenqiang Ma[1,5,9,10,11*]

Polymeric scaffolds are revolutionizing therapeutics for blinding disorders affecting the outer retina, a region anatomically and functionally defined by light-sensitive photoreceptors. Recent engineering advances have produced planar scaffolds optimized for retinal pigment epithelium monolayer delivery, which are being tested in early-stage clinical trials. We previously described a three-dimensional scaffold supporting a polarized photoreceptor monolayer, but photoreceptor somata typically occupy multiple densely packed strata to maximize light detection. Thus, patients with severe photoreceptor degeneration are expected to extract greater benefits from higher-density photoreceptor delivery. Here, we describe the microfabrication of a biodegradable scaffold patterned for high-density photoreceptor replacement. The "ice cube tray" structure optimizes mechanical properties and cell-to-biomaterial load, enabling production of a multicellular photoreceptor layer designed for outer retinal reconstruction. Our approach may also be useful in the production of a multitude of micro- and nanoscale structures for multilayered cell delivery in other tissues.

INTRODUCTION

Photoreceptors (PRs) are light-sensitive cells that capture photons to initiate electrochemical impulses that traverse a complex neural network and ultimately confer visual function. Outer retinal degenerative diseases and injuries are characterized by primary or secondary PR loss with resulting severe vision loss. These conditions are common (affecting tens of millions worldwide) (*1*, *2*), devastating, and irreversible since the human retina is incapable of intrinsic self-repair. While gene therapies hold promise for some affected patients (*3*), they are limited in scope to a small number of individuals with specific inherited retinal diseases (IRDs) who are early enough in their course to retain a sufficient amount of functional native PRs. Patients with acquired PR disorders and those in the later stages of IRDs are unlikely to benefit from these approaches (*4*, *5*). Furthermore, IRDs can be caused by mutations in more than 200 different genes (*6*), underscoring the difficulty of treating patients using gene- or mutation-specific strategies alone. Hence, widely applicable approaches for restoring vision—and, in particular, cell replacement strategies—are highly attractive as they have the potential to reach a broad patient population even at later stages of degeneration (*7*).

Advances in stem cell biology and scale-up of differentiation protocols have rapidly moved cell replacement therapies toward the clinic. Diseases of the eye and outer retina have led the way (*8*) due in part to ease of surgical access, relative immune privilege, availability of noninvasive monitoring techniques, potential for high-acuity vision replacement with a low cellular dose, and relative safety of ocular surgical interventions compared to other organs and tissues (*9*). Twelve years have passed since the first three-dimensional culture protocol for generating outer retinal cells from human pluripotent stem cells (hPSCs) was described (*10*), but the field has already reached a substantial milestone with the initiation of more than 15 clinical trials that use hPSC-derived retinal cells (*9*). All major retinal cell types can be produced from hPSCs with protocols mirroring human retinal development (*11*); however, particular weight has been placed on the generation of PRs, owing to their position at the apex of visual function and their susceptibility to degenerative processes.

The first clinical trials for outer retinal cell replacement began with hPSC–retinal pigment epithelium (RPE) cells injected as a dissociated cell suspension bolus. These phase 1/2 trials revealed shortcomings of this approach including cell reflux at the time of delivery and disorganization of the donor RPE in the subretinal space (SRS), leading to poor long-term survival and integration (*12*). Notably, cell reflux from the SRS (a potential space between the PR and RPE layers of the outer retina) into the vitreous cavity via the surgical retinotomy site can also lead to adverse patient outcomes such as epiretinal membrane formation, proliferative retinopathy, and retinal detachment (*12*, *13*). In an effort to address these challenges and to promote more precise cell placement, multiple scaffold designs have been developed and studied to date. Three hPSC-RPE planar scaffolds—including a nonbiodegradable parylene membrane, a slowly biodegradable polyethylene terephthalate scaffold, and a biodegradable poly(lactic-*co*-glycolic acid) electrospun scaffold—are currently being tested in clinical trials for hPSC-RPE monolayer delivery in patients with age-related macular degeneration (AMD) (*12*). Early reports from these studies support, in principle, the safety and feasibility of delivering scaffolds into the SRS, but these scaffolds are restricted in application to patients with salvageable native PRs. Preclinical studies aimed at hPSC-derived PR replacement have

[1]Department of Electrical and Computer Engineering, University of Wisconsin–Madison, Madison, WI 53706, USA. [2]Wisconsin Institute for Discovery, University of Wisconsin–Madison, Madison, WI 53715, USA. [3]Department of Comparative Biomedical Sciences, University of Wisconsin–Madison, Madison, WI 53706, USA. [4]Waisman Center, University of Wisconsin–Madison, Madison, WI 53705, USA. [5]McPherson Eye Research Institute, University of Wisconsin–Madison, Madison, WI 53705, USA. [6]Department of Biomedical Engineering, University of Wisconsin–Madison, Madison, WI 53715, USA. [7]Morgridge Institute for Research, Madison, WI 53715, USA. [8]Department of Ophthalmology and Visual Sciences, University of Wisconsin–Madison, Madison, WI 53705, USA. [9]Department of Materials Science and Engineering, University of Wisconsin- Madison, WI 53706, USA. [10]Department of Engineering Physics, University of Wisconsin- Madison, WI 53706, USA. [11]Grainger Institute for Engineering, University of Wisconsin- Madison, WI 53706, USA.
*Corresponding author. Email: mazq@engr.wisc.edu (Z.M.); dgamm@wisc.edu (D.M.G.); shaoqingong@wisc.edu (S.G.)
†These authors contributed equally to this work.

largely been limited to subretinal transplantation of dissociated mixed cell suspensions or whole or partial retinal organoids (*14*). A growing body of evidence from these animal studies suggests that, similar to dissociated hPSC-RPE cell transplantation, bolus injections of hPSC-PRs often suffer from reflux during transplantation, poor cell survival, structural disorganization, and/or low integration rates (*5*, *14*).

Solid and porous polymeric thin-film scaffolds supporting hPSC-derived neural retina cell growth have been developed in recent years to overcome problems inherent to bolus cell suspension injections (*15*–*26*). Despite these advances, two of the core engineering challenges these scaffolds are intended to address—cell disorganization and low or unpredictable cell payloads—have remained largely unsolved. We recently developed a "wineglass" design scaffold that succeeded in orienting a single layer of individually spaced hPSC-PRs (*26*). However, this design did not support the close association of multiple layers of hPSC-PRs and, overall, demonstrated a high burden of synthetic biomaterial relative to the cell payload. A need therefore exists for strategies to deliver dense populations of PRs to a discrete region of the retina, particularly for macular diseases that affect high-acuity central vision such as AMD. With these primary engineering goals in mind, we developed an ultrathin biodegradable scaffold patterned with micrometer-level precision, constructed specifically to improve cell payload and reduce biomaterial burden (i.e., the volume of biomaterial used to generate a single 5-mm-diameter scaffold with a thickness of 30 μm), while maintaining optimal mechanical properties for subretinal applications. Here, we describe (i) the development and optimization of the three-dimensional (3D) microstructure shape and size (i.e., scaffold design), (ii) the scaffold fabrication processes (i.e., scale-up manufacturing), (iii) the formulation and curing of the elastomeric stamp (i.e., material optimization), and (iv) the cell seeding method, leading to the production of an hPSC-PR patch aimed at reconstructing the outer neural retina.

RESULTS AND DISCUSSION

The second-generation PR scaffold design

We sought to engineer a biocompatible and biodegradable scaffold capable of capturing a high density of PRs. In the retina of humans and other vertebrates, PR cell bodies are exclusively found in the outer nuclear layer (ONL), which is approximately 8 to 10 cell nuclei in thickness and approximately 30–50 μm in height, with PR cell densities ranging from tens of thousands to hundreds of thousands per mm^2 in the macular region of healthy human retinas (*27*–*31*). In designing the scaffold, we drew upon our previous experience with the first-generation scaffold having wineglass-shaped cell capture wells (*26*). While the wineglass PR scaffold introduced key advancements in biomaterial scaffold engineering, including the potential to promote PR polarization, its cell-carrying capacity was low (1 to 2 cells per well) in comparison to the relatively high volume of synthetic biomaterial (Table 1). Therefore, an "ice cube tray"–shaped scaffold was designed as a second-generation scaffold to maximize cell payload while also reducing the overall biomaterial burden (Table 1 and fig. S1). Specifically, our second-generation scaffold was composed of two layers: (i) a reservoir layer (i.e., cell capture well layer) in which PRs are seeded and (ii) a base layer with regularly placed through-holes to facilitate fluid and nutrient transport (Fig. 1A) (*32*). Reservoirs were designed to have sufficient volume and height (i.e., length/width/height of 29/29/25 μm) to enable the capture of multiple PRs in an individual reservoir. Furthermore, to promote cell seeding inside the wells as opposed to along the top of the walls, we designed the reservoir wall width as thin as possible (~3 μm) while retaining structural integrity. Similarly, to prevent cells (which average 6 μm in diameter) from escaping through the perforated base layer, we also minimized the through-hole diameter (~5 μm). The desired scaffold thickness was near that of the native macular ONL (~30 μm), which is also consistent with recent arguments that scaffolds with a thickness of less than 50 μm can enable interactions between seeded neuroretinal cells and the host RPE (*30*, *33*, *34*).

Table 1. Structural and mechanical specifications for wineglass and ice cube tray scaffolds.

	Wineglass scaffold design (*26*)	Ice cube tray scaffold design
Overall thickness (μm)	25	30
Space between through-holes (μm)	16	10
Through-holes (μm)	5 diameter, 10 depth (1 hole per capture well)	5 diameter, 5 depth (9 holes per capture well)
Capture well reservoir volume (mm^3)	0.177×10^{-5}	2.103×10^{-5}
Scaffold biomaterial volume (based on a 5-mm-diameter scaffold) (mm^3)	0.34	0.169 (50% less biomaterial)
Young's modulus	1.18 MPa	1.3 MPa

Biomaterial selection for scaffold fabrication

Desirable retinal scaffold characteristics include the use of fully biodegradable materials having mechanical properties compatible with those of the human retina, both of which are important for clinical translation. The retina has a Young's modulus of only 0.02 MPa (*35*), making this tissue extremely flexible and fragile. A higher modulus (>1 MPa) has been shown to enhance surgical handling of RPE scaffolds (*36*) without sacrificing safety or performance following implantation in the SRS. We thus sought to develop a scaffold with a Young's modulus slightly above 1.0 MPa, balancing the need for rigidity during transplantation with flexibility to conform to the curvature of the eye upon delivery. The ideal biomaterial and its degradation products should also have proven compatibility with retinal tissue so as not to induce damage to surrounding host cells in vivo. Furthermore, the scaffold material must form thin (ideally <50 μm to facilitate interactions with RPE) (*33*), stable films and be amenable to the formation of precise, 3D PR capture well geometries during the micromolding process. Poly(glycerol sebacate) (PGS) was selected as the biomaterial of choice due to its retinal biocompatibility (*37*, *38*), known degradation behavior in the SRS (<30 to 60 days) (*38*, *39*), and suitable Young's modulus (1.18 to 1.66 MPa) (*26*, *39*). PGS undergoes gradual hydrolytic and enzymatic degradation to generate sebacic acid and glycerol, both of which are natural mammalian metabolites that are fully eliminated via physiologic mechanisms (*39*, *40*). Lastly, PGS provides the ideal combination of relatively rapid degradation in vivo with slow degradation in vitro

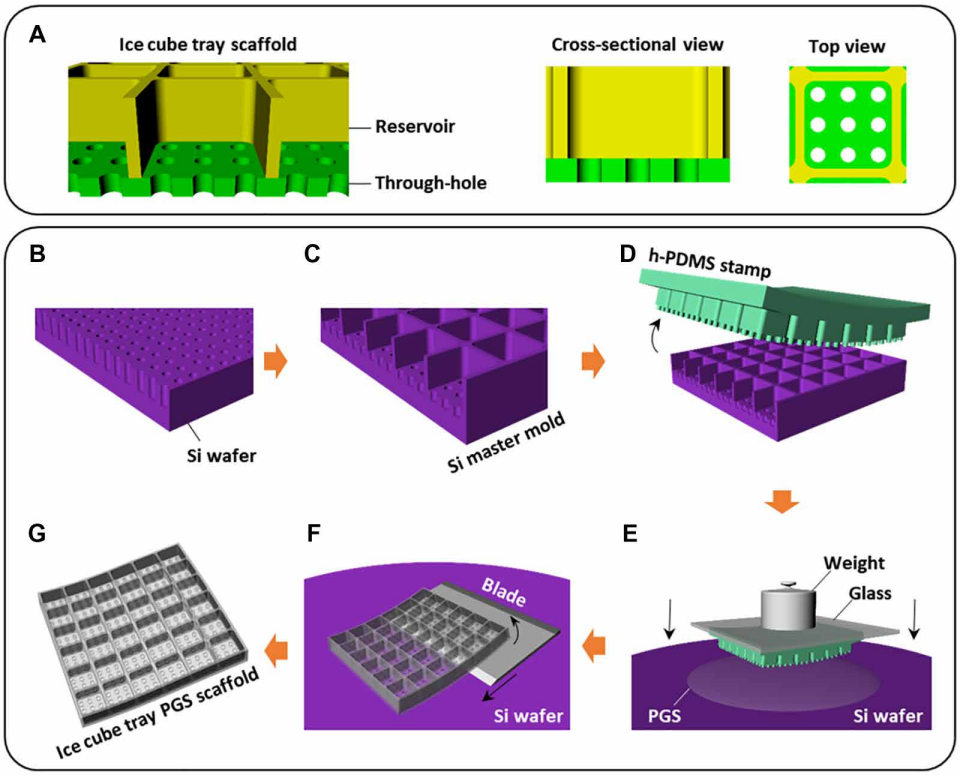

Fig. 1. PGS ice cube tray scaffold manufacturing process. (**A**) Schematic illustration of the ice cube tray PR scaffolds designed to have a reservoir layer for cell capture and retention and a through-hole layer for exchange of fluid, waste products, and nutrients both in vitro and during scaffold degradation in vivo. (**B** to **G**) Schematic illustration of the procedure to fabricate the ice cube tray PR scaffolds using a poly(glycerol sebacate) (PGS) prepolymer. (B) Through-hole and (C) reservoir etching processes of a Si master mold. (D) Molding and demolding processes of a hard-polydimethylsiloxane (h-PDMS) stamp from the Si master mold. (E) Mounting and demounting processes of the h-PDMS stamp for fabricating a PGS ice cube tray PR scaffold. (F) Delamination process of the scaffold using a razor blade. (G) Final PGS ice cube tray PR scaffold.

(*39*). We did not observe scaffold degradation after hPSC-PR seeding for up to 30 days in culture (*26*), which offers a wide time window to seed and maintain scaffolds while making arrangements for transplantation.

PGS ice cube tray PR scaffold fabrication

With the aforementioned desirable characteristics in mind, the second-generation outer retinal scaffold with an ice cube tray structure was produced using microfabrication and micromolding techniques, which are among the most promising approaches currently used in drug and cell delivery systems (*41*, *42*). Figure 1 (B to G) depicts the process workflow for fabricating PGS ice cube tray PR scaffolds. First, to fabricate a reusable silicon (Si) master mold with two distinctly patterned layers, we created a dense array of Si microstructures (through-holes and reservoirs) using photolithography and deep reactive ion etching (DRIE), a highly anisotropic etch process optimal for creating steep-sided holes or trenches in Si wafers (Fig. 1, B and C) (*43*). Here, during the DRIE process, RIE-lag effect and microloading effect were manipulated to achieve desired structure dimensions. RIE-lag effect refers to the dependency of etch rate on feature size (e.g., smaller features result in slower etch rates), while the microloading effect describes the relationship between local etch rate and pattern density (i.e., features in areas of high pattern density experience more competition for reactants, leading to a gradient in reactant flux and slower etch rate) (*44*). While generating the Si master mold, through-holes underwent two etching steps: a primary etching step and a secondary etching step (fig. S2). The etch rates of the through-holes in each step differed due to the microloading effect, with the primary etch rate and the secondary etch rate set at 2.148 and 1.746 μm/min, respectively. On the other hand, reservoirs only went through the secondary etching step, and the etch rate of the reservoirs was 2.448 μm/min, which was higher than the primary etch rate of the through-holes (i.e., 2.148 μm/min) due to the RIE-lag effect caused by the difference in feature size. By considering these effects and precisely calculating the etch rates, the desired target depths, approximately 5 μm for the through-hole layer and 25 μm for the reservoir layer, were successfully achieved (Fig. 2A). The final Si master mold included a base layer of through-holes with a diameter of 5.1 μm and a depth of 4.8 μm and a secondary layer of cuboidal (i.e., ice cube tray) reservoirs with a dimension of 29 μm by 29 μm by 24.5 μm. The width of the reservoir walls and the distance between adjacent through-holes were 2.8 and 5 μm, respectively, meeting the target dimensions. To facilitate smooth molding and demolding in the next fabrication step (Fig. 1D), we coated the fabricated Si master mold with a chemically inert passivation layer. Plasma polymerization was conducted with octafluorocyclobutane (C_4F_8) as a precursor by DRIE, generating a Teflon-like polymer film with long linear $(CF_2)_n$ chains (*45*).

Next, to create a reusable elastomeric stamp (i.e., a negative master mold for the fabrication of the final scaffold) that would not deform,

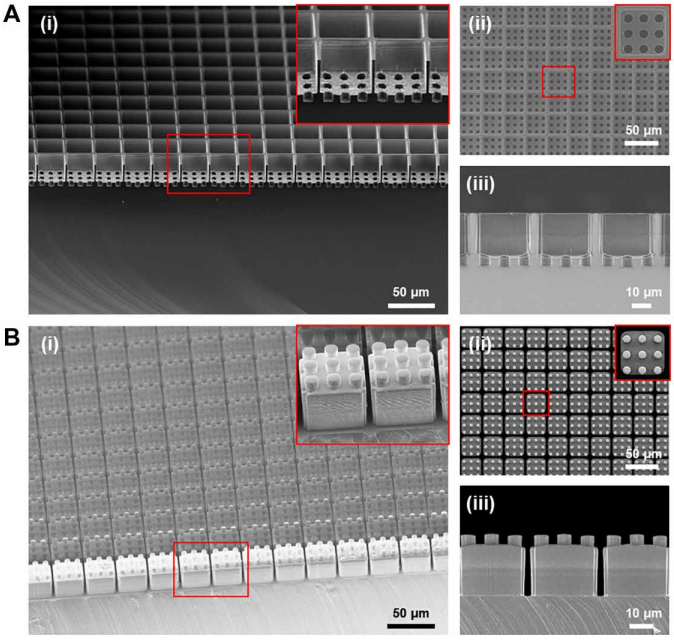

Fig. 2. Fabrication of Si master mold and h-PDMS stamp. Scanning electron microscopy (SEM) images of the ice cube tray–shaped (**A**) Si master mold, and (**B**) h-PDMS stamp showing (i) a tilted view, (ii) a top view, and (iii) a cross-sectional view, respectively. The inset images show a magnified view of the microstructures of the fabricated Si master mold and h-PDMS stamp.

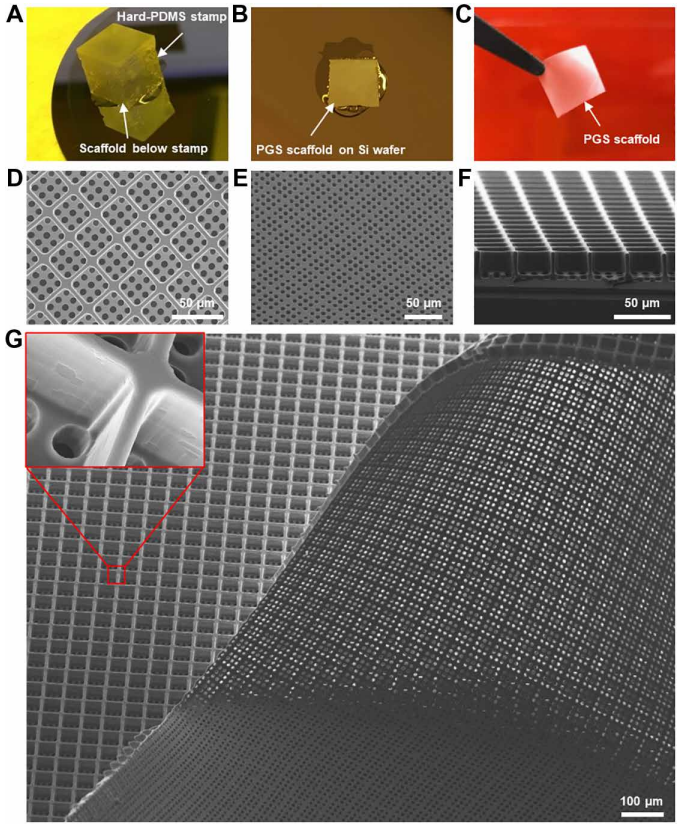

Fig. 3. Fabrication of the PGS ice cube tray PR scaffold. (**A** to **C**) Low-magnification photographic images depicting the fabrication process of the PGS ice cube tray PR scaffold. (A) h-PDMS stamp ready to be demounted from the scaffold on a Si wafer after complete PGS curing. (B) A PGS scaffold on the Si wafer after stamp removal. After removing scaffold edges, the scaffold was delaminated from the Si wafer using a single-edge razor blade. (C) Fabricated PGS ice cube tray scaffold held with fine forceps. (**D** to **G**) SEM images of the fabricated ice cube tray retinal scaffold showing (D) a top view, (E) a bottom view, and (F) a cross-sectional view. (G) Large-area SEM image of the fabricated scaffold and a magnified view of a scaffold reservoir wall (inset).

bend, or buckle during the molding process (Fig. 1E), we selected polydimethylsiloxane (PDMS) as the ideal material. Soft-PDMS stamps were initially tested, but these were frequently deformed during the demounting process due to the adherent nature of soft PDMS (fig. S3). Hard PDMS (h-PDMS) proved sufficiently strong to serve as the optimal stamp material. To create the stamp, we poured liquid h-PDMS over the fabricated Si master mold and left to cure for 12 hours at room temperature, followed by 2 hours at 60°C. After curing, the stamp was carefully demolded from the Si master mold without large surface defects, producing a high yield (>95%) of the desired ice cube tray microstructures (Fig. 2B). The stamp surface was coated with a monolayer of hydrophobic silane (an anti-adhesive layer) under vacuum to facilitate demounting from the final PGS scaffold. The microfabrication processes for the Si master mold and h-PDMS stamp are described in greater detail in Materials and Methods.

Figure 1 (E and F) depicts the final steps in the micromolding process for fabricating the ice cube tray PR scaffold from a PGS prepolymer with the h-PDMS stamp. First, PGS prepolymer was placed on a clean Si wafer and melted on a hot plate at 120°C. The micropatterned surface of the h-PDMS stamp was then immersed into the liquid PGS. A glass slide with an overlying weight of 380 g was placed atop the stamp, pressing the liquid PGS between the h-PDMS stamp and the Si wafer (Fig. 1E) to control the scaffold thickness (fig. S4). The scaffold microfabrication apparatus was subsequently placed into a vacuum oven and cured under high vacuum (<1 mbar) at 120°C for 3 days. Figure 3A shows a cured PGS scaffold between the h-PDMS stamp and the Si wafer before demounting. After curing was complete, the h-PDMS stamp was demounted from the Si wafer, taking care to avoid fractures of the h-PDMS ice cube tray microstructures due to the rigid nature of h-PDMS. Fabricated PGS scaffolds were evaluated via scanning electron microscopy (SEM) to screen for surface defects attributable to the demounting process.

Despite careful handling, early microfabrication experiments often resulted in the retention of fractured h-PDMS microstructures in the final scaffold product, rendering the h-PDMS stamp inoperable for further use (fig. S5). To address this challenge, we used isopropyl alcohol (IPA) soaking, as it allows polymers to swell and can facilitate release from secondary mold structures (*46*). The h-PDMS stamp, cured PGS, and Si wafer were incubated in IPA at room temperature for 12 hours, allowing IPA to permeate the PGS scaffold. Using this approach, the PGS scaffold on a Si wafer could be reliably demounted from the h-PDMS stamp without surface defects or retained h-PDMS stamp microstructures (Fig. 3B), maintaining the h-PDMS stamp surface integrity for reuse (fig. S6). Thereafter, the PGS scaffold was carefully delaminated from the Si wafer using a single razor blade (Fig. 1F) and unrolled with sonication treatment in IPA. The microfabrication process was subsequently optimized to produce a scaffold with minimal biomaterial burden and sufficient structural integrity for successful delamination (fig. S7). The final micropatterned ice cube tray scaffold is shown via a schematic

(Fig. 1G) and low-magnification photography (Fig. 3C). To assess microstructure quality and uniformity in the final product, we imaged the scaffolds with SEM; top, bottom, and cross-sectional views of the fabricated scaffold revealed precise, neat, and uniform ice cube tray reservoirs with the desired through-hole structures in the base of the scaffold (Fig. 3, D to F). In particular, the microstructure surfaces were smooth with no irregular or elevated edges and minimal structural defects. Furthermore, the final scaffold product had a high microstructure yield (>98%) over a large area (Fig. 3G). A detailed description of the fabrication process for ice cube tray PGS scaffolds can be found in Materials and Methods. Together, the optimized fabrication process for the ice cube tray design achieves a finely tuned balance between three critical and interrelated design criteria: target dimension, minimized biomaterial burden, and structural integrity.

Mechanical compliance of PGS ice cube tray PR scaffolds

Since the eye is spherical in shape and outer retinal scaffolds necessarily experience internal and external stresses during delivery to the SRS, an ideal PR scaffold must be not only flexible enough to conform to curved surfaces but also durable enough to withstand local stresses without structural deformation. In addition, the scaffold should return to its original form when local stresses are removed to protect and maintain proper organization of captured cells. To model this, we assessed the mechanical properties of the PGS ice cube tray PR scaffold via finite element analysis and compared them to those of our original wineglass PR scaffold (*26*) to elucidate mechanical benefits and trade-offs of each design (Fig. 4).

To determine how the scaffolds with two different designs (wineglass versus ice cube tray) behave under external stresses, we set a fixed constraint to a square area in the center of each design that incorporated nine through-holes. Thereafter, 5 N of tensile force per unit area was applied to the four sides of each scaffold in the *x* and *y* directions. As presented in Fig. 4A, the wineglass design had high stress concentrations along the boundary of the fixed constraint, leading to a change in the shape of the scaffold. In contrast, the resulting stress was uniformly and efficiently distributed throughout the ice cube tray scaffold, without causing any appreciable deformation of the scaffold (Fig. 4B), although the ice cube tray design had a higher stress than the wineglass design due to its thinner through-hole layer (i.e., 5 μm versus 10 μm), which largely determines the mechanical properties of the scaffolds because the reservoir layer only consists of very thin reservoir walls (i.e., ≤3 μm). Tensile strength and elastic modulus were also measured to assess the ice cube tray scaffold's mechanical properties. The modulus of the ice cube tray scaffold was 1.3 MPa, and all microstructures recovered to their original shapes after the tensile stress was removed (fig. S8), indicating favorable pliability for any surgical handling associated with transplantation. These results convincingly demonstrated that the ice cube tray design has superior mechanical properties compared to the wineglass design, both in terms of uniformity of stress distribution and extent of scaffold deformation under a defined tensile stress, two factors that are key for safe and consistent scaffold delivery in vivo.

Scaffold sterilization, stability, and degradation

To facilitate cell seeding, we incorporated scaffolds into a commercially available 12-mm polyester transwell cell culture insert (Corning Costar Snapwell, Sigma-Aldrich) before sterilization (Fig. 5, A to C). To mount scaffolds into the insert, we used a 5-mm biopsy punch to create a round hole in the center of the polyester transwell membrane, which is the approximate diameter of the human macula (*27*). Scaffolds were then mounted in the center of the transwell membrane and secured with soft PDMS as an adhesive (Fig. 5A). Transwell inserts were snapped into holders (Fig. 5B) and placed in a six-well plate (Fig. 5C). Scaffolds were treated with O_2 plasma to enhance the surface hydrophilicity and, thus, microstructure wettability, preventing microbubbles from forming within each capture well (fig. S9) and promoting uniform cell seeding in the capture wells (*26*, *47*, *48*).

Scaffolds were subsequently gas sterilized with ethylene oxide (fig. S10), a process widely used to sterilize delicate medical devices due to its compatibility with a variety of heat- or pressure-sensitive materials (*49*). In addition, gas sterilization does not melt the tissue

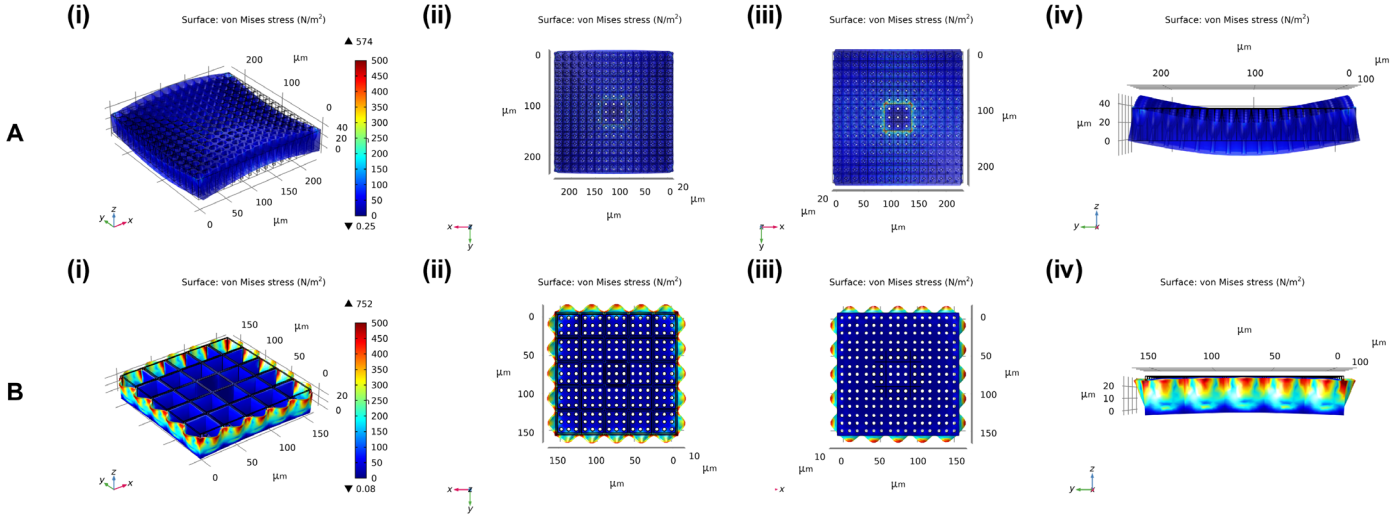

Fig. 4. Finite element analysis showing equivalent von Mises stress distribution in the PGS scaffolds. (**A**) Wineglass and (**B**) ice cube tray design under 5 N of tensile force in the *x* and *y* directions: (i) isometric view, (ii) top view, (iii) bottom view, and (iv) orthogonal view. The color bar shows the von Mises stress (in newton per square meter) for an applied tensile force.

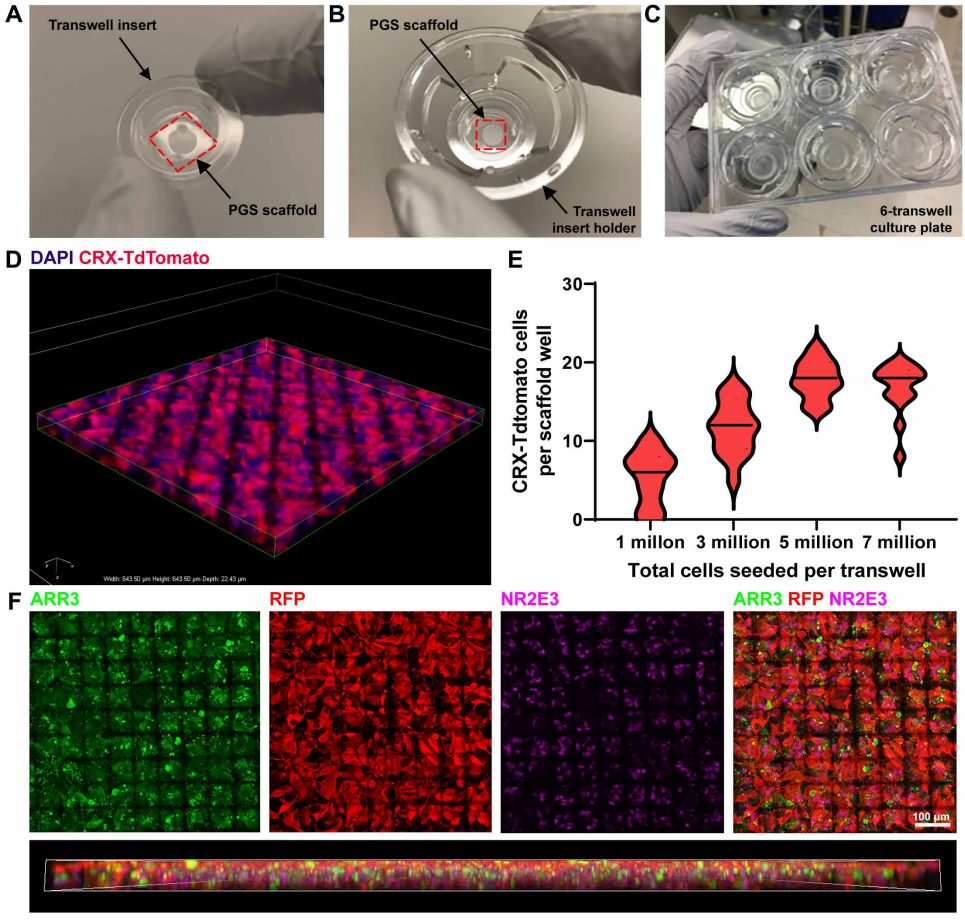

Fig. 5. Generation of PGS ice cube tray PR scaffold constructs. (**A** to **C**) Low-magnification photographic images depicting scaffold mounting into the transwell insert. (A) Transwell insert with PGS scaffold below. The outer edge of the scaffold was glued to the transwell insert with soft PDMS. The area of the transwell insert removed to mount scaffolds was 19.6 mm^2 (internal diameter, 5 mm). (B) Transwell insert holder with a PGS ice cube tray scaffold mounted into a transwell insert. (C) Six-transwell scaffold cell culture system. (**D** to **F**) Laminin-coated ice cube tray scaffolds are readily filled with hPSC-derived $CRX^{+/tdTomato}$-expressing PRs. (D) 3D rendering of a scaffold (176 μm by 185 μm by 22 μm) confirms successful capture of multiple PRs (labeled in red) in individual capture wells. Cell nuclei are labeled with 4′,6-diamidino-2-phenylindole (DAPI) (blue). (E) Cells were seeded onto scaffolds at varying densities to determine the minimum number required to achieve the maximum carrying capacity of $CRX^{+/tdTomato}$-PRs per well. Median (bold dashes) and quartiles (fine dashes) are shown within individual violin plots. (F) Scaffolds seeded with $CRX^{+/tdTomato}$-PRs (RFP^+, red) contain both ARR3-expressing cone PRs (green) and NR2E3-expressing rod PRs (pink). A 3D lateral view of the scaffold demonstrates relatively even distribution of $ARR3^+$ cones and $NR2E3^+$ rods. 3D rendering is 644 μm by 644 μm by 20 μm. Photo Credit: In-Kyu Lee, Department of Electrical and Computer Engineering, University of Wisconsin–Madison.

culture plastic housing the scaffolds, as occurs during autoclaving. Sterilized scaffolds were pretreated with an extracellular matrix protein substrate (human recombinant Laminin 521, BioLamina) previously shown to optimally facilitate hPSC-PR adhesion in similar culture systems (*26*).

To assess in vitro stability, we monitored scaffolds more than 6 weeks in culture via optical coherence tomography (OCT) imaging. During this time, scaffolds did not appreciably degrade, remaining at 100 ± 5.4% of baseline thickness at the 6-week time point. Scaffold degradation within the SRS of nude rats was also examined. Comparable to previously published PGS studies (*38*, *39*), scaffold thickness steadily decreased to 12.6 ± 3.5% of starting scaffold thickness by 2 months after implantation (fig. S11).

PR cell seeding in ice cube tray scaffolds

To assess the performance of the PGS ice cube tray PR scaffold in vitro, we used an established protocol to generate retinal organoids from a previously characterized human embryonic stem cell reporter line (WA09-$CRX^{+/tdTomato}$) that fluorescently labels PRs throughout differentiation and maturation (*50*). WA09-$CRX^{+/tdTomato}$ retinal organoids were differentiated to late stage 2 (approximately D120 of differentiation) (*11*) to achieve peak PR differentiation before seeding (*11*, *50*). Retinal organoids were then dissociated to produce a cell suspension containing a high percentage (60 to 80%) of fluorescent $CRX^{+/tdTomato}$-PRs. Laminin-coated scaffolds were seeded with cell suspensions at several concentrations (1 million, 3 million, 5 million, or 7 million cells per transwell) and cultured for 5 days to assess biocompatibility and determine the minimum number of cells necessary to achieve maximal scaffold carrying capacity (Fig. 5, D and E). Confocal imaging of fixed, immunostained scaffolds confirmed successful seeding and survival of multiple $CRX^{+/tdTomato}$-expressing PRs in individual wells of laminin-coated PGS ice cube tray scaffolds (Fig. 5D). As shown in Fig. 5E, maximal scaffold carrying capacity (17.8 ± 2.4 $CRX^{+/tdTomato}$-PRs per well or 1.74 ± 0.24 × 10^5

$CRX^{+/tdTomato}$-PRs/mm^2) could be achieved by seeding at a concentration of 5 million cells per transwell (total area of transwell, 467 mm^2) (Table 2). An optimized seeding concentration of 5 million cells per transwell was thus used for all subsequent experiments. These experiments revealed that the ice cube tray design enabled a 3.4-fold increase in cell-carrying capacity (calculated with eqs. S1 and S2) compared to the original wineglass-shaped PR scaffold design (Table 2). The ice cube tray scaffold also facilitated the capture of a multicellular layer of PRs up to three cell layers thick (average, 2.6 ± 0.7 nuclei layers per well). The differentiated PRs expressed cone-specific (cone arrestin; ARR3) and rod-specific (NR2E3) proteins as expected for hPSC-PRs derived from stage 2 retinal organoids (Fig. 5F) (*11*). The substantial increase in the cell payload capacity of the ice cube tray design, combined with its decreased overall biomaterial burden, which was 50% less for the ice cube tray design than the wineglass design (calculated with eq. S3), further underscores its relative superiority (Tables 1 and 2). These results represent the highest-density capture of hPSC-PRs for any retinal scaffold described to date. Furthermore, this construct provides a means of exceeding the often-cited threshold of 150,000 PRs within a single scaffold (Table 2), which is the threshold theoretically needed to achieve an electroretinographic response (*14*, *51*).

PR organization within PGS ice cube tray scaffold constructs

Given the importance of cell packing, organization, and polarization within the retina, particularly with regard to cones [the Stiles-Crawford effect (*52*) and the Nyquist limit (*53*) are tied to outer segment orientation and cone density, respectively], we sought to determine whether the ice cube tray scaffold design facilitated preorganization of hPSC-PRs within scaffold constructs. To assess PR polarity and scaffold construct organization, we screened whole mounts of PGS ice cube tray scaffolds seeded with 5 million cells per transwell for the presence of (i) outer segments (specialized light-detecting structures situated apically within PRs) and (ii) presynaptic vesicles, which localize to the basal PR axon terminal (Fig. 6). 3D reconstructions of scaffold flat mounts were analyzed to determine the primary location of outer segments and presynaptic terminals. $CRX^{+/tdTomato}$-PRs in scaffolds expressed peripherin (PRPH2) (Fig. 6, A and C), a protein crucial to the development of rod and cone outer segments (*54*) that contain photosensitive opsins. $PRPH2^+$ PR outer segments oriented perpendicularly to the base of the scaffold (Fig. 6C). $CRX^{+/tdTomato}$-PRs also expressed vesicular glutamate transporter 1 (VGLUT1), a presynaptic marker expressed within PR axon terminals (Fig. 6, B and D), which was primarily localized to the top half of the scaffold in 3D reconstructions (Fig. 6D). In the wineglass design, PR axons tended to extend into the through-holes, with presynaptic markers localized at the base of the scaffold. The reversal in PR polarity seen with the ice cube tray design could be due to its substantially shorter through-hole length compared to the wineglass design (5 μm versus 10 μm). Alternatively, the clustering of multiple PRs within a single well may provide local cell-cell interactions that are not present in the wineglass scaffold design. Regardless of the mechanism, a substantial benefit of the PR polarity within the ice cube tray scaffold is the greater exposure area of donor PR axon terminals at the top of the scaffold, immediately adjacent to the dendritic terminals of host interneurons (i.e., bipolar cells). Such an orientation not only minimizes barriers at the donor-host synaptic interface (before degradation of the biomaterial) but also positions the through-holes in the scaffold base to allow fluid and material exchange between the donor PRs and the host RPE and choroid as the scaffold degrades over time. It also concentrates the bulk of the biomaterial volume adjacent to the host RPE, the cell layer that plays a role in scaffold degradation

Table 2. Cell payload advantages of ice cube tray versus wineglass scaffold designs.

	Wineglass scaffold design (*26*)	Ice cube tray scaffold design
Average number of PRs per capture well	1.3 ± 0.5	17.8 ± 2.4
PRs within a single scaffold (5 mm in diameter or 19.63 mm^2)	1.005×10^5	3.412×10^5
Scaffold PR density (cells/mm^2) (6.0×10^4 to 20.0×10^4 cells/mm^2 within the macula in healthy retina)	0.512×10^4	1.74×10^4

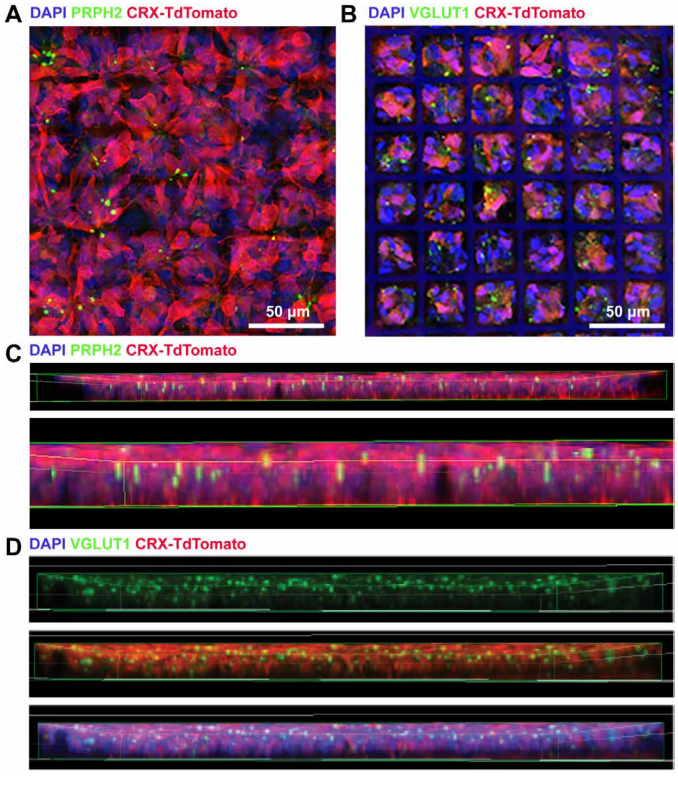

Fig. 6. Micropatterned ice cube tray scaffolds support prearranged orientation of seeded PRs. (**A** and **B**) Maximum intensity projections of scaffold whole mounts seeded with $CRX^{+/tdTomato}$-PRs (red) revealed that PRs plated on scaffolds express PRPH2 (6A, green) and VGLUT1 (6B, green). DAPI-labeled cell nuclei and PGS autofluorescence are shown in blue. (**C**) $PRPH2^+$ outer segments were often oriented perpendicular to the base of the scaffold (magnified in underlying image). (**D**) Expression of presynaptic marker VGLUT1 (green) primarily localizes to the top portion of the scaffold. 3D renderings (C and D) are 644 μm by 644 μm by 20 μm.

within the SRS (*55*), possibly due to secretion of extracellular matrix–remodeling matrix metalloproteases (*56*).

In conclusion, we have described state-of-the-art microfabrication and micromolding processes for generating biodegradable, microstructured, ultrathin scaffolds that support the formation of a dense layer of hPSC-derived PRs. Analysis of the scaffold's mechanical properties reveals favorable advances in the uniformity of stress distribution and the extent of deformation for optimal scaffold handling in downstream surgical applications. Furthermore, in vitro experiments underscored the potential of ice cube tray scaffolds to serve as an organized delivery system for more than 300,000 hPSC-PRs in a single 5-mm-diameter (19.63 mm^2) scaffold (approximately the area of the human macula, see eq. S2). PGS ice cube tray PR scaffolds exhibited not only a higher cell payload capacity and decreased biomaterial burden but also optimal donor PR orientation for integration in transplantation studies. We expect that hPSC-PRs delivered on PGS scaffolds will be better poised to survive and function after transplantation and will prevent or eliminate cell reflux and disorganization. Future studies will be aimed at assessing scaffold-mediated delivery in small and large animal models of outer retinal disease and damage, exploring minimally invasive surgical approaches, and optimizing manufacturing strategies for scale-up and good manufacturing practice production of PR-seeded scaffolds. In addition, the scaffold micromolding and microfabrication strategies developed here may prove useful for high-density, layered, and oriented cell replacement in other tissues throughout the body.

MATERIALS AND METHODS

Materials

(7.0 to 8.0% vinylmethylsiloxane)-dimethylsiloxane copolymer (VDT-731), platinum-divinyltetramethyl-disiloxane complex (Pt catalyst; SIP6831.2LC), (25 to 35% methylhydrosiloxane)-dimethylsiloxane copolymer (HMS-301), and (tridecafluoro-1,1,2,2-tetrahydrooctyl) trichlorosilane (SIT8174.0) were purchased from Gelest Inc. (USA). 2,4,6,8-Tetramethyl-2,4,6,8-tetravinylcyclotetrasiloxane, glycerol, sebacic acid, acetone, and IPA were obtained from Sigma-Aldrich Inc. (USA). All reagents were used as received without further purification.

Fabrication of silicon master mold

An undoped Si wafer was used as a starting material. After a standard RCA cleaning process, an array of through-hole patterns was formed by photolithography using an AZ2020 photoresist and etched with DRIE. During the DRIE process, etch/passivation cycles, etch/passivation time per cycle, platen power, inductively coupled plasma power, and $SF_6/O_2/C_4F_8$ gas flows were 33/33 cycles, 10/5 s, 11.7 W, 600 W, and 102/12/100 standard cubic centimeters per minute (sccm), respectively. The diameter and depth of the etched through-holes were 5.1 and 11.8 μm, respectively (fig. S12). After removing the photoresist with organic solvents (acetone and IPA), the reservoir was formed by the same procedure used for the through-hole patterning and etching, except that the DRIE etch/passivation cycles were 60/60 cycles, respectively. For the fabricated Si master mold, the diameter and depth of through-holes were 5.1 and 4.8 μm, respectively, and the length, width, and depth of reservoirs were 29, 29, and 24.5 μm, respectively. The width of reservoir wall and the distance between adjacent through-holes were 2.8 and 5 μm, respectively. After the master mold was cleaned with organic solvents and piranha solution, it was treated with oxygen plasma (Unaxis 790 RIE) for 20 s at a plasma power of 40 W, a pressure of 120 mtorr, and an oxygen gas flow rate of 20 sccm to remove the remaining organic contaminants. Last, to coat a chemically inert passivation layer on the Si master mold, plasma polymerization was conducted with C_4F_8 as a precursor by DRIE (C_4F_8, 97 sccm; time, 1 min), generating a Teflon-like polymer film with long linear $(CF_2)_n$ chains (*45*).

Fabrication of h-PDMS stamp

The h-PDMS was prepared by mixing and degassing 17 g of vinyl PDMS prepolymer (VDT-731), 90 μl of a Pt catalyst (SIP6831.2LC), 250 μl of 2,4,6,8-tetramethyl-2,4,6,8-tetravinylcyclotetrasiloxane, and 5 g of a hydrosilane prepolymer (HMS-301). Then, the h-PDMS mixture was poured onto the fabricated Si master mold and cured at room temperature for 12 hours, followed by 2 hours inside an oven at 60°C. Thereafter, the stamp was gently demolded from the master mold and cut with a single-edge razor blade to obtain nine sets of 1 cm by 1 cm by 1 cm cubes. After the stamp was cleaned with IPA, it was treated with O_2 plasma using RIE at a plasma power of 40 W, a working pressure of 120 mtorr, and a flow rate of 30 sccm for 20 s to facilitate subsequent hydrophobic silane coating (anti-stick coating). Then, the stamp was placed in a desiccator with a beaker containing 400 μl of (tridecafluoro-1,1,2,2-tetrahydrooctyl) trichlorosilane (SIT8174.0) and pumped down for 12 hours at room temperature to allow the stamp's surface to be fully functionalized by the evaporated silane. Last, the stamp was rinsed with IPA again and gently blow-dried using nitrogen.

PGS prepolymer synthesis

The PGS prepolymer was synthesized according to previously published protocols (*26*, *39*, *40*). Briefly, equimolar glycerol (4.60 g, 50 mmol) and sebacic acid (10.11 g, 50 mmol) were homogenously mixed under nitrogen atmosphere for 24 hours at 120°C. Thereafter, the reaction pressure was reduced to <1 mbar while keeping the temperature at 120°C for another 24 hours to allow further condensation polymerization. The PGS prepolymer was a white wax-like solid after it was cooled down to 20°C.

Fabrication of PGS scaffold

Approximately 10 mg of PGS prepolymer solid was placed on a clean and preheated Si wafer and melted. Then, the patterned side of the h-PDMS stamp was placed against the liquid PGS on the Si wafer. This apparatus was placed in the vacuum oven (120°C and <1 mbar) for 15 min to remove bubbles between the Si wafer and the stamp. Thereafter, a glass slide and a 380-g weight were placed on the stamp to press it against the Si wafer to control the scaffold thickness at room temperature, and the apparatus was placed back into the vacuum oven and kept at 120°C for 72 hours under <1 mbar for complete curing of PGS. After that, the Si wafer and the stamp were soaked together in IPA for 12 hours to gently demount the stamp from the Si wafer. Once the stamp was removed, the PGS scaffold on the Si wafer was blow-dried with nitrogen gas and carefully delaminated using a single razor blade. To unroll the scaffold tangled during the delamination process and remove any residues on its surface, it was soaked in an IPA solution, followed by a sonication treatment for 20 min. Last, the PGS scaffold was transferred onto a Teflon plate using a transfer pipet, and three drops of water were added on its surface to restore the swollen PGS scaffold to its

original morphology. Last, it was carefully blow-dried with the cell reservoirs facing upward.

Mounting PGS scaffolds on transwell inserts

A 12-mm polyester transwell membrane with a central 5-mm hole was secured to the scaffold with PDMS. The scaffold was degassed in a desiccator for 5 min and cured at 60°C for 4 hours to adhere the scaffold to the transwell membrane. Then, the PGS scaffold and transwell membrane were carefully detached from the Teflon plate and mounted in a transwell insert for cell culture. Last, for better cell capture, brief (20 s) oxygen plasma treatment was carried out on the top and bottom surfaces of PGS scaffold using RIE (Unaxis 790; O_2, 30 sccm; pressure, 120 mtorr; plasma power, 40 W).

Finite element analysis

To predict the mechanical properties of the PGS wineglass and ice cube tray scaffolds, the equivalent von Mises stress distributions were numerically solved using a finite element simulation software (COMSOL Multiphysics 4.2, COMSOL Ltd.). A nonlinear elastic Neo-Hookean model was used to characterize the mechanical properties, and the relevant material parameters used for the PGS polymer were $E = 1.3$ MPa, a density of 1060 kg/m^3, $\nu = 0.49$. Here, E is Young's modulus, and ν is Poisson's ratio.

Retinal organoid differentiation and culture

WA09-CRX$^{+/tdTomato}$ hPSCs were differentiated to stage 2 retinal organoids (~D120) using an established protocol for retinal differentiation (*11*, *50*). Briefly, pluripotent colonies were maintained in mTeSR Plus medium on Matrigel (Thermo Fisher Scientific) and lifted with ReLeSR (STEMCELL Technologies) to generate free-floating embryoid bodies (EBs). EBs were transitioned to neural induction medium [NIM; 1:1 Dulbecco's modified Eagle's medium (DMEM):F12 (Thermo Fisher Scientific), 1× minimal essential medium (MEM) nonessential amino acids (Thermo Fisher Scientific), 1× GlutaMAX (Thermo Fisher Scientific), heparin (2 mg/ml; Sigma-Aldrich), and 1% N2 supplement (Thermo Fisher Scientific)] over 4 days before receiving NIM with a pulse of bone morphogenetic protein 4 (BMP4) (R&D Systems) on day 6. EBs were plated onto Matrigel-coated plates on day 7 and gradually transitioned to retinal differentiation medium [RDM; 3:1 DMEM:F12 (Thermo Fisher Scientific), 1× MEM nonessential amino acids, 1× GlutaMAX, 1× antibiotic-antimycotic (Thermo Fisher Scientific), and 2% B27 supplement (Thermo Fisher Scientific)] after a series of half media changes in NIM to gradually reduce the BMP4 concentration over time. At approximately day 30 of differentiation, retinal organoids were manually dissected and maintained in free-floating cultures in RDM with 2% fetal bovine serum (FBS; WiCell). Retinal organoids were maintained in polyhydroxyethylmethacrylate (MilliporeSigma)–treated tissue culture flasks and fed twice weekly with RDM and 2% FBS until scaffold seeding. Organoids were monitored via epifluorescence microscopy to ensure that PR differentiation had peaked (as indicated by tdTomato fluorescence) as organoids reached stage 2 (~D120). Cultures were routinely screened for the presence of mycoplasma by polymerase chain reaction (WiCell).

Scaffold seeding and maintenance in culture

For cell seeding and scaffold organization experiments, stage 2 organoids (approximately D120 of differentiation) were dissociated enzymatically with papain (Worthington Biochemical) and seeded onto gas-sterilized scaffolds precoated with laminin 521 (0.05 mg/ml; human recombinant Laminin 521, BioLamina) in Hanks' balanced salt solution with calcium and magnesium (Thermo Fisher Scientific) and subsequently incubated for a minimum of 4 hours at 25°C to enable sufficient laminin polymerization. Cells were plated onto scaffolds in RDM and 10% FBS at a volume of ≤300 μl. Scaffolds were left undisturbed for the first 24 hours after seeding to facilitate cell adhesion and then gradually transitioned back to RDM and 2% FBS medium for scaffold maintenance. Scaffolds were maintained in culture for up to 5 days and fed daily with RDM and 2% FBS.

OCT imaging and analysis

To assess in vitro biodegradability of the PGS scaffolds, OCT was performed on three scaffolds, one seeded with hPSC-PRs and two without cells, for 6 weeks. Scaffolds were incorporated into glass-bottomed six-well plates (MatTek Life Sciences) and maintained as previously described, with the exception of brief transitions to imaging media [Hibernate E Low Fluorescence (BrainBits), 1× antibiotic-antimycotic, 2% B27 supplement, and 2% FBS] for ≤2 hours each week during OCT imaging. At 24 hours after seeding and weekly thereafter, the cell-seeded scaffold and two unseeded controls were imaged within glass-bottomed six-well plates using a Ganymede spectral domain OCT (Thorlabs). Central scaffold height was measured using calipers within the ThorImage OCT software (version 5.2.1).

Animals

Four male and female SD-Foxn1 Tg(S334ter)3Lav rats (*57*) (age, 1 to 4 months) were used. Animal studies were reviewed and approved by the University of Wisconsin–Madison (UW-Madison) Institutional Animal Care and Use Committee. All animals were handled in accordance with the Association for Research in Vision and Ophthalmology statement for the use of animals in Ophthalmic and Vision Research, the National Institutes of Health (NIH) Guide for the Care and Use of Laboratory Animals, and the laws of the United States and regulations of the Department of Agriculture.

Scaffold implantation in rodents

One-millimeter round PGS scaffolds were obtained using a sterile trephine punch (Electron Microscopy Sciences) and implanted into nude rats using a previously published approach for subretinal scaffold delivery in rodents (*36*). Briefly, rats were anesthetized with intraperitoneal ketamine (80 mg/kg) and xylazine (10 mg/kg), and eyes were treated with mydriatic (1% tropicamide and 2.5% phenylephrine HCl) and topical anesthetic (0.5% tetracaine HCl) ophthalmic solutions before scaffold delivery. Eyes were proptosed, coated with Goniovisc (Dynamic Diagnostics International), and covered with a coverslip to visualize scaffold entry. A scleral incision was made with a 23G MVR knife, and a subretinal bleb was raised with sodium hyaluronate viscoelastic (Abbott Medical Optics). Internal limiting membrane forceps were used to gently guide a 1-mm scaffold punch into the SRS.

Histology

Rats were humanely euthanized at 1 week, 2 weeks, 1 month, or 2 months after implant, and eyes were fixed in 4% paraformaldehyde for 1 hour to prepare tissue for histology. Eyes were placed in 30%

sucrose overnight and frozen in blocks of OCT for cryosectioning at 25 μm. Single-plane ×20 magnification images of cryosections with degrading subretinal scaffolds were acquired via differential interference contrast microscopy and analyzed in ImageJ. Fifteen evenly spaced individual measurements of scaffold thickness (measured perpendicular to the scaffold base) were obtained from one to three cryosections per eye. Thickness was reported as the mean percentage of starting scaffold thickness (±SD) and graphed using GraphPad Prism.

Immunocytochemistry and confocal imaging

Scaffolds seeded with hPSC-PRs were fixed in 4% paraformaldehyde for 30 min, washed in 1× phosphate-buffered saline (PBS; Thermo Fisher Scientific) and processed for immunocytochemistry as previously described to assess expression and localization of PR-specific proteins (*26*). Briefly, scaffold whole mounts were incubated in blocking solution [10% normal donkey serum (Abcam), 5% bovine serum albumin (MilliporeSigma), and 0.5% Triton X (MilliporeSigma) in 1× PBS] for 1 hour at room temperature, followed by overnight incubation at 4°C in primary antibodies. Scaffolds were washed with 1× PBS to remove residual primary antibody solution before incubating for 30 min at room temperature in secondary antibodies at 1:500 (Alexa Fluor 488, Alexa Fluor 545, and Alexa Fluor 633, Thermo Fisher Scientific). After an additional round of washes in 1× PBS, scaffolds were carefully removed from transwells and mounted in Prolong Gold Antifade with 4′,6-diamidino-2-phenylindole (DAPI) mounting medium (Thermo Fisher Scientific) before coverslipping. Confocal z-stacks of immunostained scaffolds were captured at ×20 magnification with a Nikon A1R confocal microscope. 3D z-stack reconstruction, maximum intensity projection image generation, and cell capture quantification were performed with Nikon Elements software. Descriptive statistics for quantitative analyses were performed with and visualized in GraphPad Prism. Averages reported herein are identified as the means ± SD.

SUPPLEMENTARY MATERIALS

Supplementary material for this article is available at http://advances.sciencemag.org/cgi/content/full/7/17/eabf0344/DC1

REFERENCES AND NOTES

1. S. R. Flaxman, R. R. A. Bourne, S. Resnikoff, P. Ackland, T. Braithwaite, M. V. Cicinelli, A. Das, J. B. Jonas, J. Keeffe, J. H. Kempen, J. Leasher, H. Limburg, K. Naidoo, K. Pesudovs, A. Silvester, G. A. Stevens, N. Tahhan, T. Y. Wong, H. R. Taylor; Vision Loss expert Group of the Global Burder of Disease Study, Global causes of blindness and distance vision impairment 1990-2020: A systematic review and meta-analysis. *Lancet Glob. Health* **5**, e1221–e1234 (2017).
2. G. C. Cockerham, T. A. Rice, E. H. Hewes, K. P. Cockerham, S. Lemke, G. Wang, R. C. Lin, C. Glynn-Milley, L. Zumhagen, Closed-eye ocular injuries in the Iraq and Afghanistan wars. *N. Eng. J. Med.* **364**, 2172–2173 (2011).
3. A. V. Garafalo, A. V. Cideciyan, E. Heon, R. Sheplock, A. Pearson, C. WeiYang Yu, A. Sumaroka, G. D. Aguirre, S. G. Jacobson, Progress in treating inherited retinal diseases: Early subretinal gene therapy clinical trials and candidates for future initiatives. *Prog. Retin. Eye Res.* **77**, 100827 (2020).
4. M. S. Singh, S. S. Park, T. A. Albini, M. V. Canto-Soler, H. Klassen, R. E. MacLaren, M. Takahashi, A. Nagiel, S. D. Schwartz, K. Bharti, Retinal stem cell transplantation: Balancing safety and potential. *Prog. Retin. Eye Res.* **75**, 100779 (2020).
5. D. M. Gamm, R. Wong; the AGI Workshop Panelists, Report on the national eye institute audacious goals initiative: Photoreceptor regeneration and integration workshop. *Transl. Vis. Sci. Technol.* **4**, 2 (2015).
6. S. K. Verbakel, R. A. C. van Huet, C. J. F. Boon, A. I. den Hollander, R. W. J. Collin, C. C. W. Klaver, C. B. Hoyng, R. Roepman, B. J. Klevering, Non-syndromic retinitis pigmentosa. *Prog. Retin. Eye Res.* **66**, 157–186 (2018).
7. D. A. Thompson, R. R. Ali, E. Banin, K. E. Branham, J. G. Flannery, D. M. Gamm, W. W. Hauswirth, J. R. Heckenlively, A. Iannaccone, K. T. Jayasundera, N. W. Khan, R. S. Molday, M. E. Pennesi, T. A. Reh, R. G. Weleber, D. N. Zacks; Monaciano Consortium, Advancing therapeutic strategies for inherited retinal degeneration: Recommendations from the monaciano symposium. *Invest. Ophthalmol. Vis. Sci.* **56**, 918–931 (2015).
8. J. H. Stern, Y. Tian, J. Funderburgh, G. Pellegrini, K. Zhang, J. L. Goldberg, R. R. Ali, M. Young, Y. Xie, S. Temple, Regenerating eye tissues to preserve and restore vision. *Cell Stem Cell* **22**, 834–849 (2018).
9. M. Zarbin, Cell-based therapy for retinal disease: The new frontier. *Methods Mol. Biol.* **1834**, 367–381 (2019).
10. J. S. Meyer, R. L. Shearer, E. E. Capowski, L. S. Wright, K. A. Wallace, E. L. McMillan, S.-C. Zhang, D. M. Gamm, Modeling early retinal development with human embryonic and induced pluripotent stem cells. *Proc. Natl. Acad. Sci. U.S.A.* **106**, 16698–16703 (2009).
11. E. E. Capowski, K. Samimi, S. J. Mayerl, M. J. Phillips, I. Pinilla, S. E. Howden, J. Saha, A. D. Jansen, K. L. Edwards, L. D. Jager, K. Barlow, R. Valiauga, Z. Erlichman, A. Hagstrom, D. Sinha, V. M. Sluch, X. Chamling, D. J. Zack, M. C. Skala, D. M. Gamm, Reproducibility and staging of 3D human retinal organoids across multiple pluripotent stem cell lines. *Development* **146**, dev171686 (2019).
12. R. Sharma, D. Bose, A. Maminishkis, K. Bharti, Retinal pigment epithelium replacement therapy for age-related macular degeneration: Are we there yet? *Annu. Rev. Pharmacol. Toxicol.* **60**, 553–572 (2020).
13. J. S. Baldassarre, A. Joseph, M. Keane, J. S. Heier, Subretinal delivery of cells via the suprachoroidal space: Janssen trial, in *Cellular Therapies for Retinal Disease: A Strategic Approach*, S. D. Schwartz, A. Nagiel, R. Lanza, Eds. (Springer International Publishing, 2017), pp. 95–104.
14. S. J. Gasparini, S. Llonch, O. Borsch, M. Ader, Transplantation of photoreceptors into the degenerative retina: Current state and future perspectives. *Prog. Retin. Eye Res.* **69**, 1–37 (2019).
15. D. Singh, S.-B. Wang, T. Xia, L. Tainsh, M. Ghiassi-Nejad, T. Xu, S. Peng, R. A. Adelman, L. J. Rizzolo, A biodegradable scaffold enhances differentiation of embryonic stem cells into a thick sheet of retinal cells. *Biomaterials* **154**, 158–168 (2018).
16. W. L. Neeley, S. Redenti, H. Klassen, S. Tao, T. Desai, M. J. Young, R. Langer, A microfabricated scaffold for retinal progenitor cell grafting. *Biomaterials* **29**, 418–426 (2008).
17. T. A. E. Ahmed, R. Ringuette, V. A. Wallace, M. Griffith, Autologous fibrin glue as an encapsulating scaffold for delivery of retinal progenitor cells. *Front. Bioeng. Biotechnol.* **2**, 85 (2014).
18. M. Tomita, E. Lavik, H. Klassen, T. Zahir, R. Langer, M. J. Young, Biodegradable polymer composite grafts promote the survival and differentiation of retinal progenitor cells. *Stem cells* **23**, 1579–1588 (2005).
19. A. Shrestha, B. N. Allen, L. A. Wiley, B. A. Tucker, K. S. Worthington, Development of high-resolution three-dimensional-printed extracellular matrix scaffolds and their compatibility with pluripotent stem cells and early retinal cells. *J. Ocul. Pharmacol. Ther.* **36**, 42–55 (2020).
20. J. Yao, C. W. Ko, P. Y. Baranov, C. V. Regatieri, S. Redenti, B. A. Tucker, J. Mighty, S. L. Tao, M. J. Young, Enhanced differentiation and delivery of mouse retinal progenitor cells using a micropatterned biodegradable thin-film polycaprolactone scaffold. *Tissue Eng. Part A* **21**, 1247–1260 (2015).
21. A. C. McUsic, D. A. Lamba, T. A. Reh, Guiding the morphogenesis of dissociated newborn mouse retinal cells and hES cell-derived retinal cells by soft lithography-patterned microchannel PLGA scaffolds. *Biomaterials* **33**, 1396–1405 (2012).
22. P. Baranov, A. Michaelson, J. Kundu, R. L. Carrier, M. Young, Interphotoreceptor matrix-poly(ϵ-caprolactone) composite scaffolds for human photoreceptor differentiation. *J Tissue Eng.* **5**, 2041731414554139 (2014).
23. B. A. Tucker, S. M. Redenti, C. Jiang, J. S. Swift, H. J. Klassen, M. E. Smith, G. E. Wnek, M. J. Young, The use of progenitor cell/biodegradable MMP2-PLGA polymer constructs to enhance cellular integration and retinal repopulation. *Biomaterials* **31**, 9–19 (2010).
24. K. S. Worthington, L. A. Wiley, E. E. Kaalberg, M. M. Collins, R. F. Mullins, E. M. Stone, B. A. Tucker, Two-photon polymerization for production of human iPSC-derived retinal cell grafts. *Acta Biomater.* **55**, 385–395 (2017).
25. J. R. Thompson, K. S. Worthington, B. J. Green, N. K. Mullin, C. Jiao, E. E. Kaalberg, L. A. Wiley, I. C. Han, S. R. Russell, E. H. Sohn, C. A. Guymon, R. F. Mullins, E. M. Stone, B. A. Tucker, Two-photon polymerized poly(caprolactone) retinal cell delivery scaffolds and their systemic and retinal biocompatibility. *Acta Biomater.* **94**, 204–218 (2019).
26. Y. H. Jung, M. J. Phillips, J. Lee, R. Xie, A. L. Ludwig, G. Chen, Q. Zheng, T. J. Kim, H. Zhang, P. Barney, J. Min, K. Barlow, S. Gong, D. M. Gamm, Z. Ma, 3D microstructured scaffolds to support photoreceptor polarization and maturation. *Adv. Mater.* **30**, 1803550 (2018).
27. S. Polyak, *The Retina* (University of Chicago Press, 1941).
28. C. A. Curcio, K. R. Sloan, R. E. Kalina, A. E. Hendrickson, Human photoreceptor topography. *J Comp Neurol* **292**, 497–523 (1990).

29. B. J. Lujan, A. Roorda, J. A. Croskrey, A. M. Dubis, R. F. Cooper, J.-K. Bayabo, J. L. Duncan, B. J. Antony, J. Carroll, Directional optical coherence tomography provides accurate outer nuclear layer and henle fiber layer measurements. *Retina* **35**, 1511–1520 (2015).
30. Y. Yu, E. M. Moult, S. Chen, Q. Ren, P. J. Rosenfeld, N. K. Waheed, J. G. Fujimoto, Developing a potential retinal OCT biomarker for local growth of geographic atrophy. *Biomed. Opt. Express* **11**, 5181–5196 (2020).
31. J. B. Jonas, U. Schneider, G. O. H. Naumann, Count and density of human retinal photoreceptors. *Graefes Arch. Clin. Exp. Ophthalmol.* **230**, 505–510 (1992).
32. P.-H. Prévot, K. Gehere, F. Arcizet, H. Akolkar, M. A. Khoei, K. Blaize, O. Oubari, P. Daye, M. Lanoë, M. Valet, S. Dalouz, P. Langlois, E. Esposito, V. Forster, E. Dubus, N. Wattiez, E. Brazhnikova, C. Nouvel-Jaillard, Y. LeMer, J. Demilly, C.-M. Fovet, P. Hantraye, M. Weissenburger, H. Lorach, E. Bouillet, M. Deterre, R. Hornig, G. Buc, J.-A. Sahel, G. Chenegros, P. Pouget, R. Benosman, S. Picaud, Behavioural responses to a photovoltaic subretinal prosthesis implanted in non-human primates. *Nat. Biomed. Eng.* **4**, 172–180 (2020).
33. K. E. Kador, J. L. Goldberg, Scaffolds and stem cells: Delivery of cell transplants for retinal degenerations. *Expert Rev Ophthalmol.* **7**, 459–470 (2012).
34. M. Trese, C. V. Regatieri, M. J. Young, Advances in retinal tissue engineering. *Materials* **5**, 108–120 (2012).
35. I. L. Jones, M. Warner, J. D. Stevens, Mathematical modelling of the elastic properties of retina: A determination of Young's modulus. *Eye* **6**, 556–559 (1992).
36. R. Sharma, V. Khristov, A. Rising, B. S. Jha, R. Dejene, N. Hotaling, Y. Li, J. Stoddard, C. Stankewicz, Q. Wan, C. Zhang, M. M. Campos, K. J. Miyagishima, D. McGaughey, R. Villasmil, M. Mattapallil, B. Stanzel, H. Qian, W. Wong, L. Chase, S. Charles, T. McGill, S. Miller, A. Maminishkis, J. Amaral, K. Bharti, Clinical-grade stem cell-derived retinal pigment epithelium patch rescues retinal degeneration in rodents and pigs. *Sci. Transl. Med.* **11**, eaat5580 (2019).
37. F. Ghosh, W. L. Neeley, K. Arnér, R. Langer, Selective removal of photoreceptor cells in vivo using the biodegradable elastomer poly(glycerol sebacate). *Tissue Eng. Part A* **17**, 1675–1682 (2009).
38. S. Redenti, W. L. Neeley, S. Rompani, S. Saigal, J. Yang, H. Klassen, R. Langer, M. J. Young, Engineering retinal progenitor cell and scrollable poly(glycerol-sebacate) composites for expansion and subretinal transplantation. *Biomaterials* **30**, 3405–3414 (2009).
39. R. Rai, M. Tallawi, A. Grigore, A. R. Boccaccini, Synthesis, properties and biomedical applications of poly(glycerol sebacate) (PGS): A review. *Prog. Polym. Sci.* **37**, 1051–1078 (2012).
40. Y. Wang, G. A. Ameer, B. J. Sheppard, R. Langer, A tough biodegradable elastomer. *Nat. Biotechnol.* **20**, 602–606 (2002).
41. S. R. Hynes, E. B. Lavik, A tissue-engineered approach towards retinal repair: Scaffolds for cell transplantation to the subretinal space. *Graefes Arch. Clin. Exp. Ophthalmol.* **248**, 763–778 (2010).
42. H. Zhang, J. K. Jackson, M. Chiao, Microfabricated drug delivery devices: Design, fabrication, and applications. *Adv. Funct. Mater.* **27**, 1703606 (2017).
43. S. Franssila, J. Kiihamäki, J. Karttunen, Etching through silicon wafer in inductively coupled plasma. *Microsyst. Technol.* **6**, 141–144 (2000).
44. B. Wu, A. Kumar, S. Pamarthy, High aspect ratio silicon etch: A review. *J. Appl. Phys.* **108**, 051101 (2010).
45. F. Laermer, S. Franssila, L. Sainiemi, K. Kolari, Chapter 21 - Deep reactive ion etching, in *Handbook of Silicon Based MEMS Materials and Technologies (Second Edition)*, M. Tilli, T. Motooka, V.-M. Airaksinen, S. Franssila, M. Paulasto-Kröckel, V. Lindroos, Eds. (Micro and Nano Technologies, William Andrew Publishing, 2015), pp. 444–469.
46. M. J. Kim, M. Y. Hwang, J. Kim, D. J. Chung, Biodegradable and elastomeric Poly(glycerol sebacate) as a coating material for nitinol bare stent. *Biomed. Res. Int.* **2014**, e956952 (2014).
47. M. Liu, S. Wang, L. Jiang, Nature-inspired superwettability systems. *Nat. Rev. Mater.* **2**, 17036 (2017).
48. H. Jo, H. S. Park, M. H. Kim, Single bubble dynamics on hydrophobic–hydrophilic mixed surfaces. *Int. J. Heat Mass Trans.* **93**, 554–565 (2016).
49. H. Shintani, Ethylene oxide gas sterilization of medical devices. *Biocontrol Sci.* **22**, 1–16 (2017).
50. M. J. Phillips, P. Jiang, S. Howden, P. Barney, J. Min, N. W. York, L.-F. Chu, E. E. Capowski, A. Cash, S. Jain, K. Barlow, T. Tabassum, R. Stewart, B. R. Pattnaik, J. A. Thomson, D. M. Gamm, A novel approach to single cell RNA-sequence analysis facilitates in silico gene reporting of human pluripotent stem cell-derived retinal cell types. *Stem Cells* **36**, 313–324 (2018).
51. R. A. Pearson, A. C. Barber, M. Rizzi, C. Hippert, T. Xue, E. L. West, Y. Duran, A. J. Smith, J. Z. Chuang, S. A. Azam, U. F. O. Luhmann, A. Benucci, C. H. Sung, J. W. Bainbridge, M. Carandini, K.-W. Yau, J. C. Sowden, R. R. Ali, Restoration of vision after transplantation of photoreceptors. *Nature* **485**, 99–103 (2012).
52. G. Westheimer, Directional sensitivity of the retina: 75 years of Stiles–Crawford effect. *Proc. Biol. Sci.* **275**, 2777–2786 (2008).
53. J. I. Yellott, The photoreceptor mosaic as an image sampling device, in *Advances in Photoreception: Proceedings of a Symposium on Frontiers of Visual Science* (National Academies Press, 1990).
54. M. W. Stuck, S. M. Conley, M. I. Naash, PRPH2/RDS and ROM-1: Historical context, current views and future considerations. *Prog. Retin. Eye Res.* **52**, 47–63 (2016).
55. Z. Liu, N. Yu, F. G. Holz, F. Yang, B. V. Stanzel, Enhancement of retinal pigment epithelial culture characteristics and subretinal space tolerance of scaffolds with 200 nm fiber topography. *Biomaterials* **35**, 2837–2850 (2014).
56. J. P. Alexander, J. M. Bradley, J. D. Gabourel, T. S. Acott, Expression of matrix metalloproteinases and inhibitor by human retinal pigment epithelium. *Invest. Ophthalmol. Vis. Sci.* **31**, 2520–2528 (1990).
57. M. J. Seiler, R. B. Aramant, M. K. Jones, D. L. Ferguson, E. C. Bryda, H. S. Keirstead, A new immunodeficient pigmented retinal degenerate rat strain to study transplantation of human cells without immunosuppression. *Graefes Arch. Clin. Exp. Ophthalmol.* **252**, 1079–1092 (2014).

Acknowledgments: We are indebted to the following individuals who assisted with cryosectioning: A. Willes, U. Nlebedum, M. Bhadkhamkar, K. Nilles, S. Stuedemann, M. Piraino, J. Mustful, K. Schmidt, and A. Pitts. **Funding:** This work was supported by the Department of Defense through the Vision Research Program under award no. W81XWH-20-1-0655. Opinions, interpretations, conclusions, and recommendations are those of the authors and are not necessarily endorsed by the Department of Defense. This work was also supported by a Gund-Harrington Scholar Award in collaboration with the Foundation Fighting Blindness and the Harrington Discovery Institute, Bach Family Acceleration Fund in Innovation, Research to Prevent Blindness, Emmett A. Humble Distinguished Directorship of the Retina Research Foundation, McPherson Eye Research Institute Sandra Lemke Trout Chair in Eye Research, Carl and Mildred Reeves Foundation, Sarah E. Slack Prevention of Blindness Fund-Muskingum County Community Foundation, NIH grant P51OD011106 to the Wisconsin National Primate Research Center, and NIH grant U54HD090256 to the Waisman Intellectual and Developmental Disabilities Research Center. A.L.L. was supported by the UW-Madison School of Veterinary Medicine Dual DVM/PhD Program, NIH/NEI U24 EY029890, and Kirschstein NRSA Predoctoral Fellowship NIH/NEI F30 EY031230. B.S.S. was supported by the Morgridge Institute for Research Postdoctoral Fellowship Program. **Author contributions:** I.-K.L., J.L., and R.X. performed the scaffold fabrication and finite element analysis. A.L.L. and M.J.P. performed scaffold seeding and rodent experiments, immunostaining, confocal imaging, and analysis. B.S.S. performed in vitro spectral domain OCT imaging and analysis. L.D.J. assisted with rodent scaffold implantation. Figures were prepared by I.-K.L., A.L.L., J.L., M.J.P., and B.S.S. All authors contributed to the critical discussion of the experimental design, results, and interpretation. I.-K.L. and A.L.L. cowrote the original manuscript draft with input from all the authors. Z.M., S.G., and D.M.G. conceived the project and acquired funding. **Competing interests:** D.M.G. is an inventor on patents related to this work filed by the Wisconsin Alumni Research Foundation, Madison, WI (no. 9,752,119, filed 29 April 2016, published 5 September 2017) (no. 9,328,328, filed 24 August 2010, published 3 May 2016). D.M.G., Z.M., M.J.P., and S.G. are inventors on a patent filed by the Wisconsin Alumni Research Foundation, Madison, WI (no. 2017/0226459, filed 5 February 2016, published 10 August 2017). D.M.G., Z.M., J.L., M.J.P., S.G., and I.-K.L. are inventors on a patent filed by the Wisconsin Alumni Research Foundation, Madison, WI (no. 2020/0010799, filed 9 July 2019, published 9 January 2020). D.M.G. and M.J.P. have an ownership interest in Opsis Therapeutics LLC, which has licensed the technology to generate 3D optic vesicles from pluripotent stem cell sources reported in this publication. The authors declare that they have no other competing interests. **Data and materials availability:** All data needed to evaluate the conclusions in the paper are present in the paper and/or the Supplementary Materials. The WA09-CRX$^{+/tdTomato}$ hPSC reporter line is available upon request and is subject to a materials transfer agreement. Additional data related to this paper may be requested from the authors.

Submitted 1 October 2020
Accepted 4 March 2021
Published 21 April 2021
10.1126/sciadv.abf0344

Citation: I.-K. Lee, A. L. Ludwig, M. J. Phillips, J. Lee, R. Xie, B. S. Sajdak, L. D. Jager, S. Gong, D. M. Gamm, Z. Ma, Ultrathin micromolded 3D scaffolds for high-density photoreceptor layer reconstruction. *Sci. Adv.* **7**, eabf0344 (2021).